OPTICAL PROPERTIES OF MONAZITE NANOPARTICLES PREPARED VIA BALL MILLING

Abstract

This research work focused on the preparation of Monazite nanoparticles using ball milling technique and the determination of its optical properties. High energy ball milling was used to prepare nanoparticles from the bulk materials using the top-down technique. Debye–Scherer formula was used to determine the crystalline size of the nanoparticle. Optical properties such as transmittance, refractive index, extinction coefficient, optical conductivity and band gap energy were determined. The result showed that the crystalline size was about 64.23nm on the average. The dislocation density calculated ranged from 0.149 x 10^{-3}nm to 0.460 x 10^{-3}nm. The absorbance decreased as the wavelength spectrum moved from the ultraviolet region to the visible region and the near-infrared region. The refractive index increased from 1.57 a.u to 2.65 a.u as the photon energy increased from about 1.38eV to 1.14eV. The transmittance at the near-infrared region was even up to 90.9% in some cases. The band energy gap was between 3.57eV and 4.11eV. The properties of the Monazite nanoparticles determined showed that it can have possible applications in optoelectronic and photovoltaic devices.

Keywords: Monazite, nanoparticle, optical properties, crystalline size, bend energy gap, refractive index

1. Introduction

Nanoparticles are usually products of nanotechnology whose particle size is less than 100nm (Prerna et al. 2021; Mhadhbi 2021, Adam et al. 2016). They are smaller than everyday objects described by Newton's laws but bigger than atoms/molecules described by quantum mechanics. Nanoparticles are the fundamental components in the creation of nanostructure of substances. They are basically small particle-sized objects that act as a whole unit in accordance with their transport and properties. The properties of most materials change as their size move towards the atomic scale. Hence, metallic nanoparticles have significant different physiochemical properties with respect to their bulk metallic material (Satoshi and Nick, 2013). This is because the surface

area to volume ratio will increase leading to the surface atoms of the materials now dictating the performance of the materials.

The development of improved nanoparticle materials is gaining global attention among scientists because of the numerous applications of the materials. Currently, there is ongoing extensive research on the preparation of the essential and vital third generation semiconductor nanoparticles that have comprehensive relevance on account of their multi-functional characteristics (Faramawy et al. 2022). These nanoparticles have copious importance in semiconducting industries, optoelectronic industries and photocatalytic industries (Madkhali et al. 2022). Furthermore, they can be applied in the environmental field for water treatment, gas sensors, solar photocatalysis, etc (Theerthagiri et al. 2019; Hamid et al. 2017; Kumar et al. 2015); in electro-optical fields for solar cells, optical waveguides, light-emitting devices etc (Hwang et al. 2007); in biological fields for biomedical and antibacterial purposes, biosensors etc (Tereshchenko et al. 2016); in electronics for light emitting diode, thin film transistors, etc (Kumar et al. 2015). Furthermore, nanoparticles have been reported to have applications in photocatalysis (Fen, et al. 2007), Solar cells (Martinson et al. 2007), UV protectors (Wang et al. 2005), gas sensing devices (Yang et al. 2006)

The wide application of nanoparticles is based on their desired properties which is usually different from the bulk material. Most nanoparticles have large energy gap, excellent provision of ultraviolet emissions with an acceptable exciton binding energy (Rong et al. 2018). Furthermore, they have significant stability level and capacity to modify electrical conductivity of gases with intrinsic ability to absorb UV radiations (Madkhali et al. 2022; Liu et al. 2011)

Generally there are two major methods of nanoparticles preparation namely: top-down (break down) method and bottom-up (build up) method (Satoshi and Nick, 2013). The top down method involves the application of an external force on a much reduced bulk solid material that results to its breaking down into smaller particles of nano-size. The bottom-up method entails the alteration and conversion of liquids or gaseous atoms through molecular condensation or atomic transformation into relatively larger particles of nano-sizes.

The top-down method involving the milling or breaking down of bulk substance into nanoparticles sizes. The milling process is appropriate for producing highly scattered

nanoparticles that ward off the condensation of the newly generated nanoparticles (Satoshi and Nick, 2013).

The ball milling is a mechanical technique where the kinetic energy of the moving balls are exerted on a much reduced material resulting to the breaking down of the chemical bonds and the production of nanoparticles (Carmen et al. 2019; Tan et al. 2013). It is a top-down nanoparticle preparation method that involves the pulverizing of the bulk solid material into powder using the energy of the kinetic motions of the impacted balls. Particles of powder are confined between colliding balls and the inner surface of the vial, causing recurring deformation and disintegration of powder leads to the formation of finer particles (Rijesh et al. 2018). This will generate nano-sized particles with new properties and new surfaces (Joy et al. 2023). In general, it is a mechanical technique whose principle can be described by the utilization of high energy grinding for the reduction of the bulk material. It is an economic, environmentally-friendly and simple top-down nanoparticle synthesis that strengthens the particles onto the surface of the composite matrix interlayers (Li et al. 2020). Furthermore, ball milling has the potential for industrial scalability in nanoparticle synthesis (Zhang *et al.,* 2022; Alami *et al.,* 2021). Hence it can have various industrial applications.

Monazite is a group of minerals that contains different compositions of different rare earth elements. The rare earth elements are majorly lanthanum, Cerium, Neodymium, Thorium among others (Schulz 2021; Anitha et al. 2020). Hence, the chemical formula of the most important Monazite specie is (Ce, La, Nd, Th)PO_4. It is known as Monazite-Ce. The Rare earth elements are important ingredients in the development of high technology products in industries (Wei et al. 2017). It is non-fluorescent with a density of about 4.8 to 5.5 g/cm^3. It is reddish brown in colour with a monoclinic crystal system. Monazite is known as a detrital mineral (Frank and Joseph, 2010). Hence, the aim of this research is to prepare nanoparticles from Monazite bulk materials and determined its crystalline and optical properties.

2. Materials and methods

2.1 Sourcing and preparation of samples

The Monazite was sourced from Dengi Local Government Area of Plateau State Nigeria. Due to its relatively large bulkiness, it was first manually crushed into fine pebbles. This is to make it amenable for the ball milling experiment.

2.2 Preparation of the nanoparticle via ball milling experiment

The ball milling experiment was carried out in a Planetary ball milling machine located in the Faculty of Engineering, Nnamdi Azikiwe University Awka, Nigeria. It has vials with steel coatings and hardened steel balls inside of about 10.0mm diameter to prepare the fine nanoparticles. The Monazite was introduced through the milling lid. The milling was done in ambient atmosphere.

A constant ball-to-powder weight ratio of 10:1 (wt/wt) was maintained during the operation. The ball milling was performed in a horizontal operation technique at 25 Hz. The milled materials were used directly with no added milling media. The ball milling was for a total of 10 hours with some time intervals which helped in avoiding undesirable rapid increase in temperature inside the milling vial. The crystal properties were used to determine the average size of the nanoparticles.

2.3 Crystalline properties of the nanoparticle

The crystalline size "D" of the nanoparticles was calculated using the Debye–Scherer formula while the dislocation density was calculated from the crystalline size.

2.4 Optical properties

2.4.1 Optical transmission spectral

The transmittance (T) of the nanoparticles was obtained from the absorbance value according to equation 1.

$$T = 10^{-A} \quad (1)$$

Where A is the absorbance value of the nanoparticle

2.4.2 Reflection spectra

The reflectance of the nanoparticles was calculated from the absorbance and transmittance spectrum using the relation equation 2

$$R = 1 - T - A \quad (2)$$

where R is the reflectance of the nanoparticle, T the transmittance and A the absorbance of the nanoparticle**.**

2.4.3 Refractive index

The refractive index (η) of the nanoparticles was calculated from reflectance values using equation 3

$$\eta = \frac{1+\sqrt{R}}{1-\sqrt{R}} \quad (3)$$

where R is the reflectance of the thin film.

2.4.4 Determination of optical conductivity

The optical conductivity of the nanoparticles was determined using equation 4.

$$\sigma = \frac{\alpha nc}{4\pi} \quad (4)$$

where, α is absorption coefficient of the material, n is the refractive index of the material, c is speed of light while π is a constant

2.4.5 Extinction coefficient

The extinction coefficient (k) of the nanoparticles was evaluated from equation 5

$$k = \frac{\alpha\lambda}{4\pi} \quad (5)$$

where α is the absorption coefficient and λ is the wavelength and π is a constant

2.4.6 Dielectric constant

The dielectric constant is composed of two parts; the real and imaginary parts. The real part of the dielectric constant relates to the dispersion while the imaginary part provides a measure of dissipative rate of the wave in the medium (Yakuphanoglu et. al., 2007).

2.4.7 Real part of dielectric constant

The real part of dielectric constant (ε_r) relates to the dispersion of the nanoparticles. It was determined using the equation 6

$$\varepsilon_r = \eta^2 - k^2 \quad (6)$$

Where η is the refractive index and k is extinction coefficient

2.4.8 Imaginary part of dielectric constant

The imaginary part of dielectric constant provides a measure of dissipative rate of the wave in the medium. It was determined using equation 7

$$\varepsilon_i = 2\ln k \quad (7)$$

where η is the refractive index and k is extinction coefficient.

2.4.9 Energy band Gap

The energy band gaps of the prepared nanoparticles was extracted from the graph of the equation 8

$$\alpha h\nu = A\left(h\nu - E_g\right)^n \quad (8)$$

Where α is the absorption coefficient, hv is the photon energy, A is a constant, E_g is the bandgap, and n is for modes of transition (1/2) for direct transition and 2 is for indirect transition).

3. Results and discussion

3.1 X-ray diffraction and crystal analysis

Some of the structural and lattice properties of the Monazite particles were evaluated from the x-ray diffraction (XRD) analysis. The full width at half maximum ranged from 0.067 to 0.180nm. The nanopatrticle distance spacing ranged from 1.63 to 3.44 Å.

The nanoparticle crystalline size was evaluated using the Debye–Scherer formula given in equation 9 (Sutapa et al. 2018; Ashraf et al. 2015)

$$D = \frac{k\,\lambda}{\beta \cos\theta} \quad (9)$$

Where, K represents the Scherrer constant usually taken as 0.9, β is full width at half-maximum (FWHM), λ is the X-ray wavelength (0.15406nm) and θ is Bragg's diffraction angle.

The Dislocation density is a function of the crystalline size and was calculated using $\frac{1}{D^2}$ (Sutapa et al. 2018). The results of some of the crystal analysis are tabulated in Tables 1. The crystalline size ranged from 46.36nm to 82.02nm with an average crystalline size of 64.23nm.The full width at half maximum showed an indirect relationship with the crystalline size.

Table 1. Crystal properties of the Monazite

2θ, °	d, Å	FWHM, ° (β)	hkl	Crystalline size (nm)	Dislocation density $(nm)^{-2}$
22.42	3.963	0.126	100	64.27578	0.000242
27.03	3.29	0.12	110	68.08784	0.000216
28.78	3.09	0.1	110	82.01602	0.000149
35.59	2.52	0.18	111	46.35263	0.000465
39.92	2.25	0.12	111	70.43325	0.000202
47.89	1.89	0.16	210	54.32747	0.000339

The dislocation density calculated ranged from 0.149 x 10^{-3}nm to 0.460 x 10^{-3}nm. The dislocation density defines the number of dislocation lines per unit volume of crystals. Since the dislocation density obtained for is small, the nanoparticles prepared have a high degree of crystallinity (Sutapa et al. 2018).

The X-ray diffraction (XRD) pattern is shown in Figure 1 respectively. Distinct peaks were observed at 2theta angles of 22.42, 27.03, 28.78, 35.59, 39.92, and 47.89 which correspond to hkl miller indices of 100, 110, 110, 111, 111, and 210 respectively on the crystallographic planes (Mbonu, 2015; Falak, 2010). Insignificant broad peaks were observed in the pattern indicating little impurities within the crystal structure. The effect of impurities on the crystal structure has a significant role in the change of the physical properties (Saleem *et. al.*, 2016).

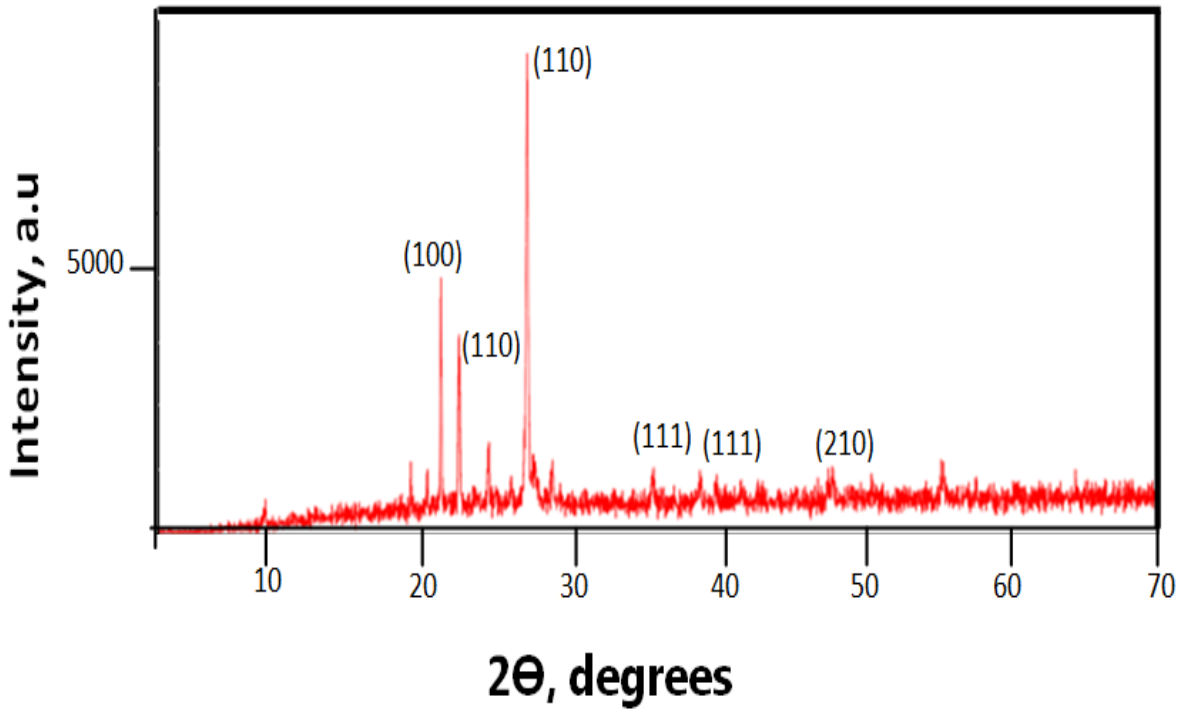

Figure 1. X-ray diffraction pattern

3.2 Absorption spectra of Monazite particles

The absorption spectra of the Monazite particle with distilled water and ethanol as the dispersing agents are shown in Figure 2. The particles exhibited relatively high absorbance within 35.3% to 44.8% at the ultraviolet region with an almost constant decrease. The absorbance decreased further towards the visible regions and the near-infrared regions even becoming less that 10% in some cases. The absorbance was near zero at the near-infrared regions indicating that the Monazite particle are non-absorbing at the near-infrared regions. Similar trend was reported by Khalid et al. (2019). Additionally, in all spectrum ranges, the particles dispersed in distilled water and ethanol showed approximately the same absorbance. In the ultraviolet and near-infrared bands, the absorbance of the particles dispersed in distilled water was just slightly greater than that of the particles dispersed in ethanol. The Monazite particle have relatively high absorbance at the visible region and hence can be utilized in several coating processes (Layth 2014).

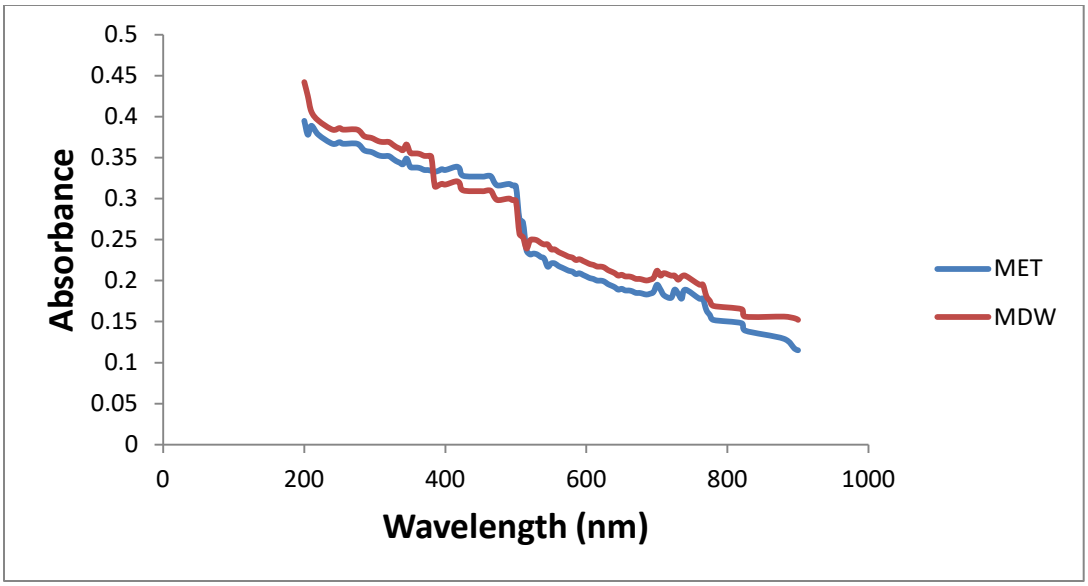

Figures 2: Plot of absorbance against wavelength

3.3 Transmittance of the Monazite nanoparticle

Figure 3 showed the transmittance spectra of the Monazite particles. The transmittance was obtained from the absorbance as the exponent of the negative value of the absorbance. The transmittances were obtained at different sizes for distilled water dispersed particles and ethanol dispersed particles. The transmittance increased from its initial value of 35.6% to 42.8% in the ultraviolet region to as high as 79% in the near-infrared region. The transmittance at the near-infrared region was even up to 90.9% in some cases. The particle showed poor transmittance in the ultraviolet area and moderately good transmittance in the near-infrared and visible parts of the spectrum. This shows that the monazite particles have good optical transmission in the near-infrared and visible spectrum areas (Layth, 2014). In addition, the high transmittance in the visible area suggests the possibility for simple photon transit, indicating the potential usefulness of monazite particles in optical materials' electron transport layers (Khalid et al., 2019). Also these results showed that the Monazite particles can be utilized in optoelectronic and photovoltaic devices (Layth, 2014).

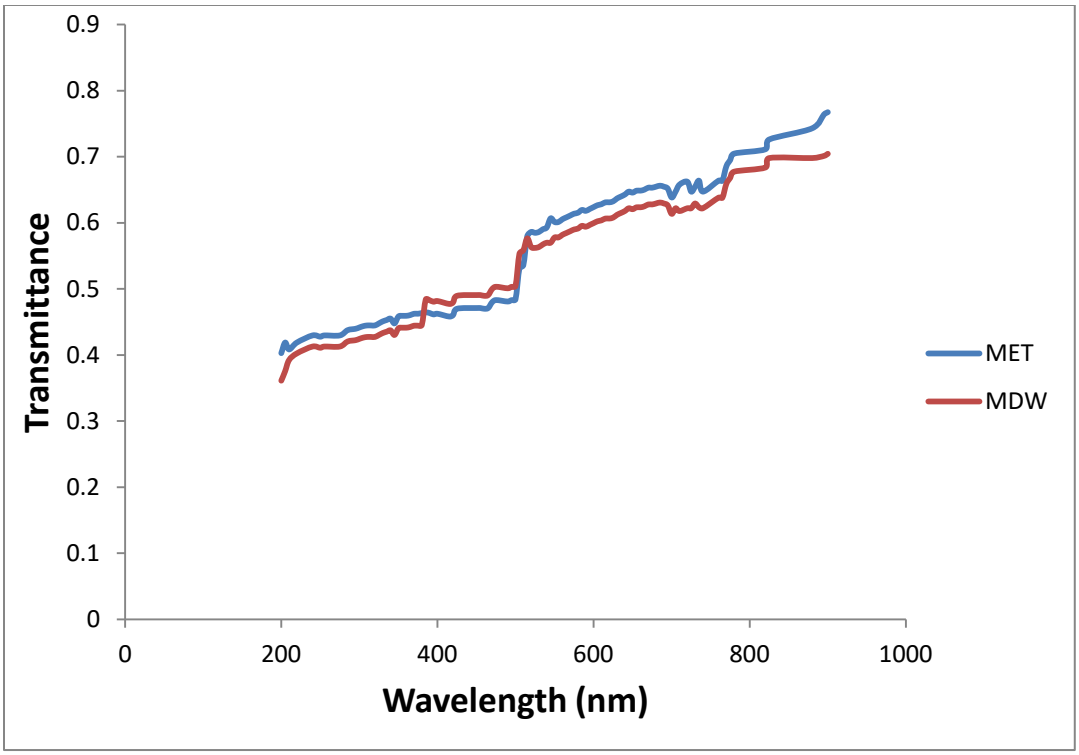

Figures 3: Plot of transmittance against wavelength

3.4 Reflectance of the Monazite nanoparticle

The variation of the reflectance of the Monazite particles with wavelength is shown in Figure 4. It depends on the transmittance and absorbance of the particle. The reflectance was ranged from 20.3% to 4.9% throughout the regions of the spectrum. According to the figures, the reflectance gradually decreased from 20.3% in the UV to 9.0% in the visible spectrum. However, when it moved towards the near-infrared spectrum, a substantial decrease was noticed, down to 14.0 to 4.9%. The plot is very similar to that of Nada (2010). Poor reflectivity over the whole spectrum assumes it can be utilized in the window layer of a solar cell. For optical applications, a very low reflectance is preferred (Wanjala et al., 2016).

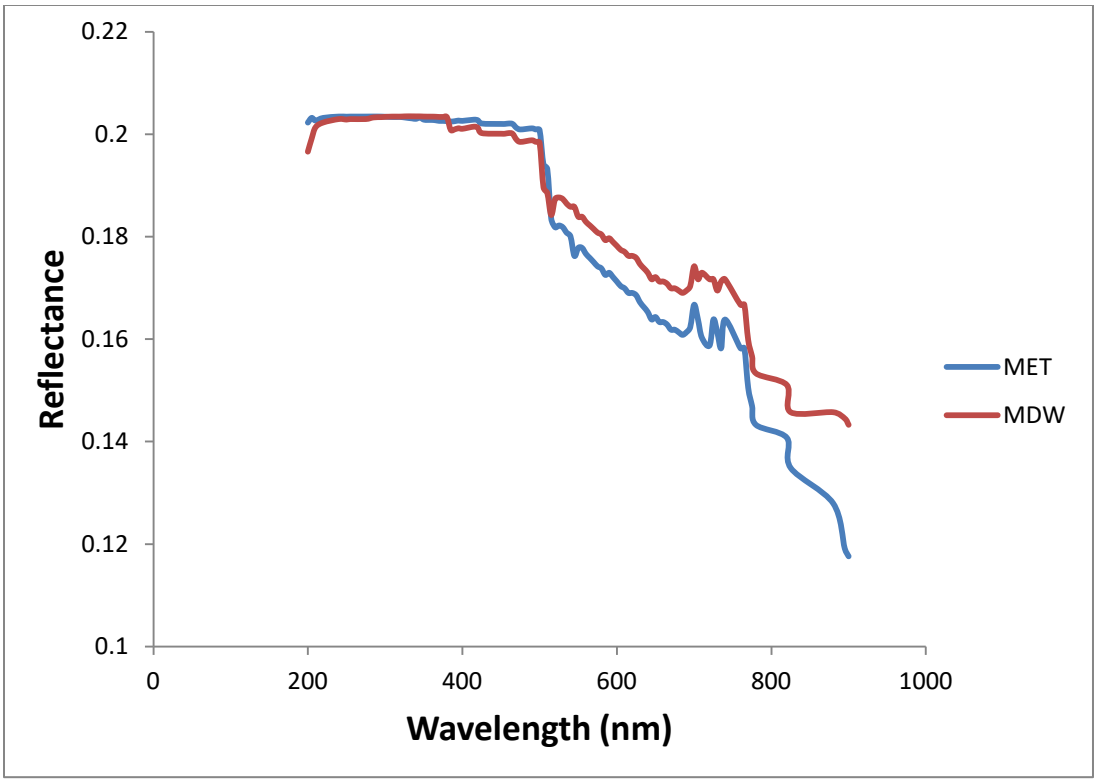

Figure 4: Plot of reflectance against wavelength

3.5 Refractive index

The plot of the refractive index of the Monazite particles as a function of photon energy was presented in Figure 5. The refractive index was evaluated from the reflectance values. The refractive index increased from 1.57 a.u to 2.65 a.u as the photon energy increased from about 1.38eV to 1.14eV and then experienced relative stability as the photon energy increased to about 6.21eV. This indicates that the refractive index of the Monazite particles can be tuned to manipulate their matrix characteristics even at molecular stage (Hiroshi et al. 2016). Refractive index depends on wavelength and moderates the interaction between the nanoparticles and light in various applications (Edwin et al. 2014). The refractive index determines the degree of the optical force that an electromagnetic field can wield on the particles. The refractive index of nanoparticles is one of the most important physical parameters used to inspect the quality of particle-based solids.

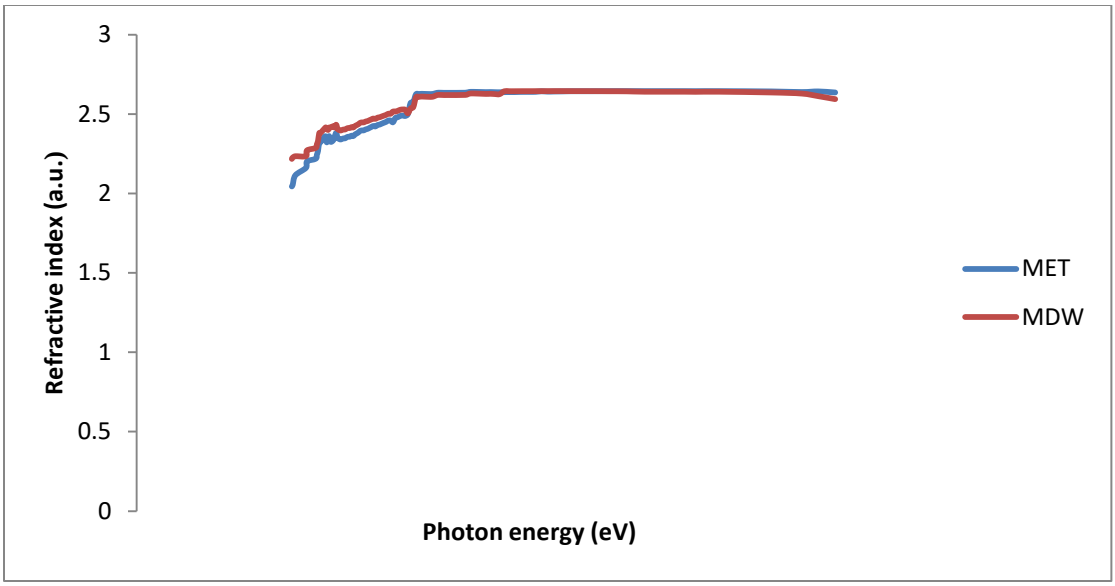

Figure 5. Plot of refractive index against photon energy

3.6 Absorption coefficient

The plots of absorption coefficient of the Monazite particles at different wavelengths were presented in Figure 6. There was an observed reduction in the absorption coefficient of the Monazite as the wavelength increased. At the near-infrared region, the absorption coefficient was almost constant with further increase in the wavelength. The ability of the Monazite films to absorb light in those regions is indicated by the high absorption coefficient of the Monazite particles at the ultraviolet region and visible region (Oluyamo and Agunbiade, 2016). The absorption coefficient describes the ability of the nanoparticle to absorb light. It is a direct function of absorbance and wavelength of the particle.

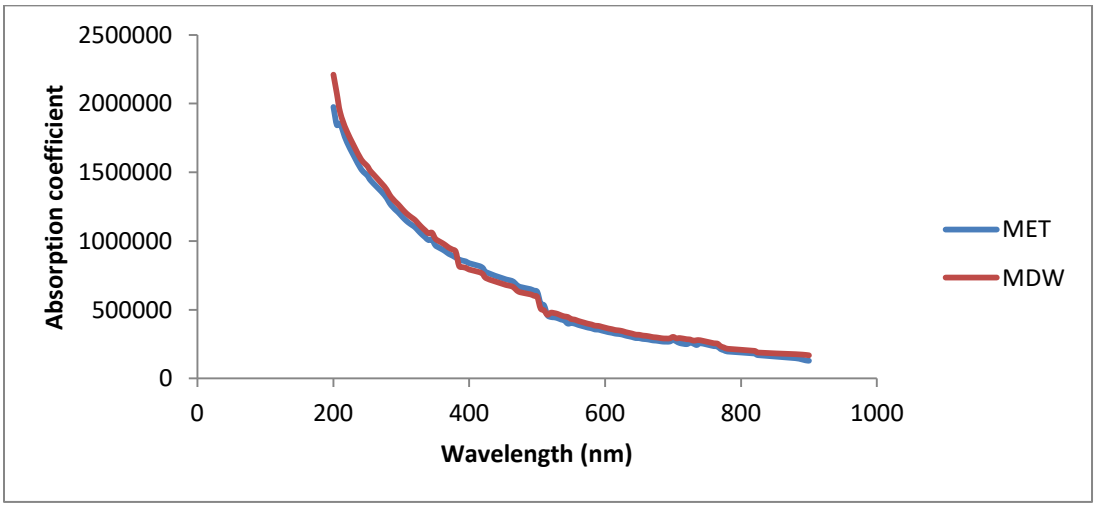

Figure 6. Plot of absorption coefficient against wavelength

3.7 Extinction coefficient

The plots of the extinction coefficients at different particle sizes are shown in Figure 7. The extinction coefficient of the Monazite particles was determined from the absorption coefficient and the wavelength. The extinction coefficient initially reduces sharply in the UV range, and then progressively declines toward the visible zone Since nanoparticles are not monodispersed, the measurement of the extinction coefficient, which is a key parameter in estimating the nanoparticle concentration, may be used to determine the molar concentration. Additionally, a relatively high extinction coefficient indicates the capacity to naturally release absorbed energy as heat rather than harmful radiation (Krohnke 2001).

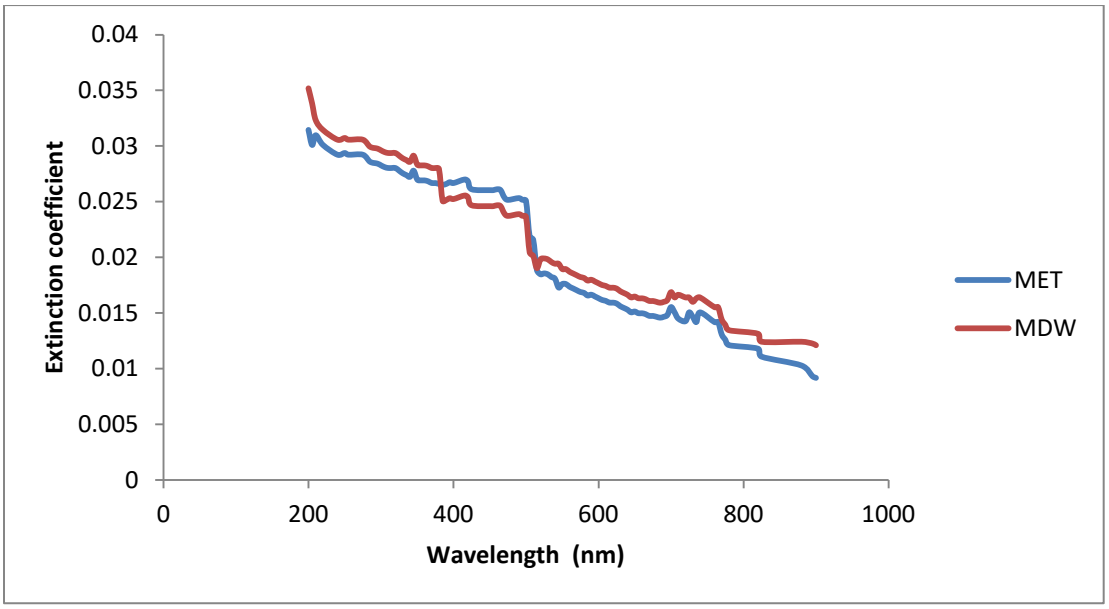

Figure 7. Plot of extinction coefficient against wavelength

3.8 Real Dielectric constant

By deducting the square of the extinction coefficient from the square of the refractive index, the real part dielectric constant was calculated. The plots of the real part dielectric constant of the Monazite particles as a function of photon energy at different particle sizes were given in Figure 8. With a rise in photon energy up to about 2.6 eV, a sharp and very erratic increase in the real part dielectric constant was observed. This increase then stabilizes until approximately 6.1 eV before suffering a modest shift once more. According to Yakuphanoglu *et al.*, (2007), the real part of the dielectric constant relates to the dispersion and is a measure of the polarization of the material.

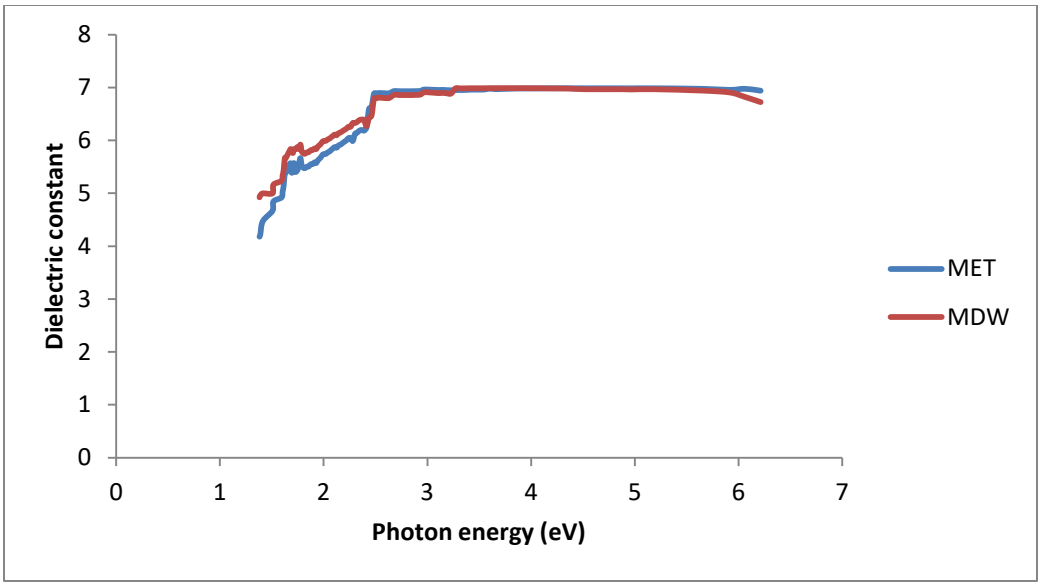

Figure 8. Plot of Real Dielectric Constant against photon energy

3.9 Imaginary Dielectric constant

The various plots of the imaginary dielectric constant of the Monazite particles against photon energy are depicted in Figure 9. Imaginary dielectric constant depends on the extinction coefficient and the refractive index. It was evaluated as twice the product of extinction coefficient and the refractive index of the particle (Noor et al. 2019). When the photon energy increased up to around 2.65 eV, an irregular increase in the real part dielectric constant was seen. The photon energy subsequently stabilized until about 3.45 eV before suffering another abrupt increase. Data on the real and imaginary portions of the dielectric constant, which is the ratio between the real and imaginary parts of the dielectric constant, offer information about the loss factor.

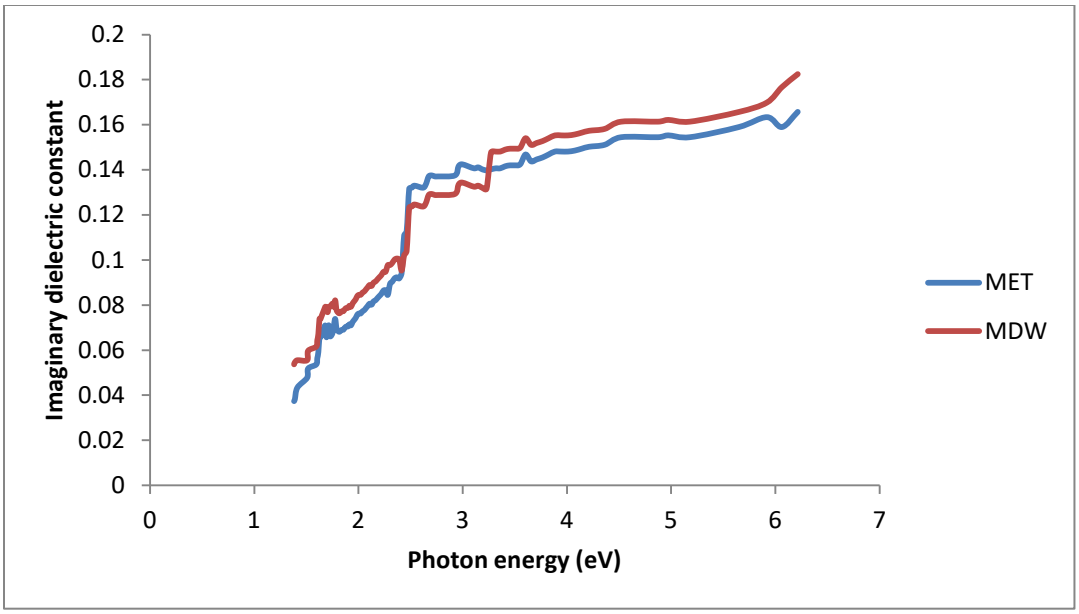

Figure 9. Plot of Imaginary Dielectric Constant against photon erengy

3.10 Optical Conductivity

The optical conductivity of the Monazite particles was determined as a function of absorption coefficient and the refractive index of the material. The plots of the optical conductivity against the photon energy are presented in Figure 10. The optical conductivity experienced an almost linear increase from 1.43 x 10^{13} s^{-1} to about 1.38 x 10^{14} s^{-1} as the photon energy increased from 1.41eV to 6.21eV. The optical conductivity shows the rate of absorption of incident photons. The connection between the current density and the material's exposure to various light wavelengths in the electric field is made possible by the optical conductivity, which is crucial in determining the atomic structure of the particle. Additionally, certain nanoparticles' spectra are determined by their optical conductivity.

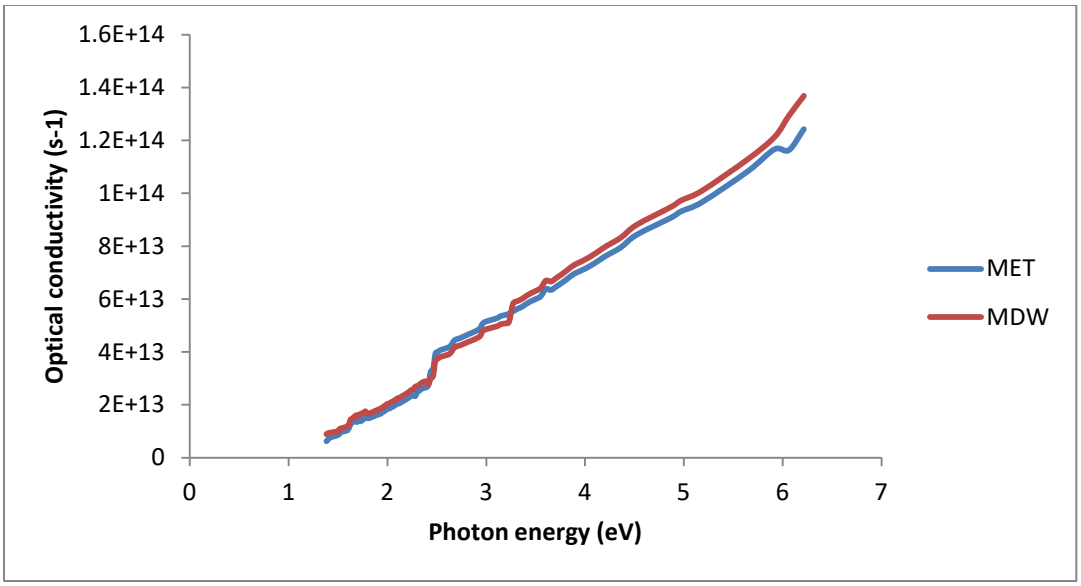

Figure 10. Plot of Optical Conductivity against photon energy

3.11 Band energy gap

The band energy gap is a crucial factor in optoelectronic instrument design. It is usually referred to as the minimum energy required to excite an electron in the conduction band where it can conduct. Figures 11 and 12 are the plots of plot of $(\alpha h\nu)^2$ versus photon energy for the Monazite particles. The band energy gap was determined by exploiting the tangential line of the plot of $(\alpha h\nu)^2$ versus photon energy (Faramawy et al. 2022). The minimum band energy obtained was 3.57eV and while the maximum was 4.11eV. The band energy gap of the Monazite particles dispersed in distilled water was marginally lower than those dispersed in ethanol. When compared with Sphalerite particles, the band energy of the Monzaite was slightly lower.

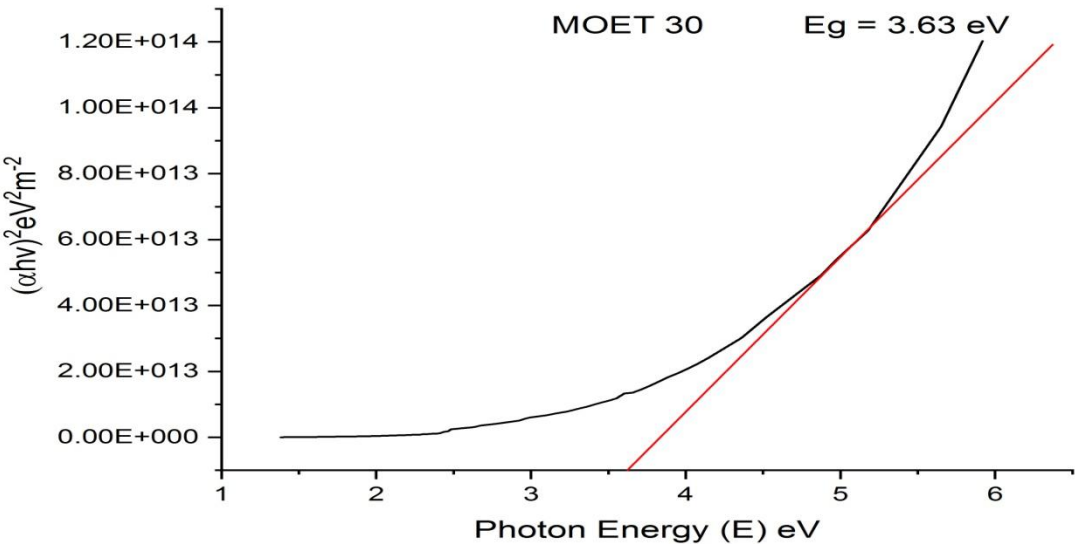

Figure 11. Plot of the band energy gap for Monazite dispersed in ethanol

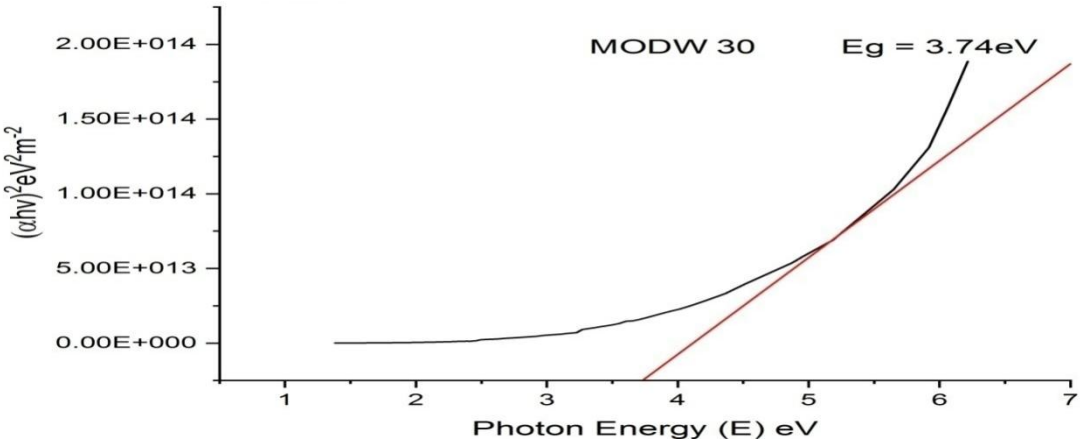

Figure 12. Plot of the band energy gap for Monazite dispersed in distilled water

4. Conclusion

In this research nanoparticles were prepared from Monazite bulk materials using high energy ball milling technique and characterized for their crystalline and optical properties. The absorbance of nanoparticle decreased as the UV spectrum moved from the ultraviolet region to the visible

region and to the near-infrared regions. The average crystalline size was 64.23nm while the dislocation density ranged from 0.149 x 10^{-3}nm to 0.460 x 10^{-3}nm. The particle showed poor transmittance in the ultraviolet area and moderately good transmittance in the near-infrared and visible parts of the spectrum. The band energy gap was 3.63eV and 3.74eV for the nanoparticle dispersed in ethanol and distilled water respectively. The optical conductivity and refractive index increased with increased in photon energy. The work showed that Monazite nanoparticles can be prepared using ball milling technique for different photovoltaic and optoelectronic devices.

References

Adam, Ż., Svitlana, S., Wiktor, K., Dariusz, B., and Katarzyna, M., (2016). Zinc sulphide (ZnS) nanparticles for advanced application Technical transactions chemistry, 125 – 134. 10.4467/2353737xct.16.053.5315

Alami, A.H., Aokal, K., Olabi, A.G., Alasad, S., and Aljaghoub, H., (2021). Applications of graphene for energy harvesting applications: Focus on mechanical synthesis routes for graphene production. Energy Sources Part A Recovery Util. Environ. Eff. 43, 1–30.

Anitha J. K., Sabu J., Rejith R. G., and Sundararajan M., (2020). Monazite chemistry and its distribution along the coast of Neendakara–Kayamkulam belt, Kerala, India. © Springer Nature Switzerland AG, Applied Sciences 2:812 | https://doi.org/10.1007/s42452-020-2594-6 2020.

Ashraf, R., Saira R., Zohra N.K., and Shahzad N., (2015). Structural and magnetic properties of iron doped ZnO nanoparticles. Materials Today: Proceedings 2, 5384 – 5389 doi:10.1016/j.matpr.2015.11.055.

Carmen, C.P., Susana, F. B., and Wim, M. D.,(2019). Ball milling: a green technology for the preparation and functionalisation of nanocellulose derivatives. Nanoscale Adv., 1, 937. DOI: 10.1039/c8na00238j.

Edwin V.D.P., Frank, A.W.C., Auguste S., Rienk N., and Ton G.V.L., (2014) Refractive Index Determination of Nanoparticles in Suspension Using Nanoparticle Tracking Analysis. ACS Nano Letter., 14, 11, 6195–6201. dx.doi.org/10.1021/nl503371p.

Falak, S. (2010) Crystal Structure Determination I. Pakistan Institute of Engineering and Applied Sciences 1 – 41.

Faramawy, A., Elsayed, H., Scian, C., and Mattei, G., (2022). Structural, Optical, Magnetic and Electrical Properties of Sputtered ZnO and ZnO:Fe Thin Films: The Role of Deposition Power. Ceramics, 5, 1128–1153. https://doi.org/10.3390/ceramics5040080.

Fen, X., Zhang, P., Navrotsky, A., Yuan, Z., Ren, T., Halasa, M., and Su, B., (2007). Hierarchically assembled porous ZnO nanoparticles: synthesis, surface energy, and photocatalytic activity. Chem Mater;19:5680.

Frank, S., Spear, J., and Pyle, M., (2010). Theoretical modeling of monazite growth in a low-Ca metapelite. Chemical Geology 273, 111–119. doi:10.1016/j.chemgeo.2010.02.016.

Hamid, S.B.A., Teh, S.J., and Lai, C.W. (2017) Photocatalytic Water Oxidation on ZnO: A Review. Catalysts, 7, 93. 1 – 14. doi:10.3390/catal7030093

Hiroshi K., Ayumu I., Katja O., Ilpo N., (2016) Refractive index measurement of nanoparticles by immersion refractometry based on a surface plasmon resonance sensor. Chemical Physics Letters, (654), 72-75. https://doi.org/10.1016/j.cplett.2016.05.013

Hwang, D.K., Oh, M.S., Lim, J.H., and Park, S.J. (2007) ZnO thin films and light-emitting diodes. J. Phys. D Appl. Phys. 2007, 40, R387–R412. **DOI** 10.1088/0022-3727/40/22/R01

Joy, J., Krishnamoorthy, A., Tanna, A., Kamathe, V., Nagar, R., and Srinivasan, S., (2022). Recent Developments on the Synthesis of Nanocomposite Materials via Ball Milling Approach for Energy Storage Applications. Appl. Sci. https://doi.org/10.3390/app12189312.

Khalid N.R., Hammad A., Tahir M.B., Rafique M., Iqbal, T., Nabi, G., and Hussain M.K., (2019) Enhanced photocatalytic activity of Al and Fe co-doped ZnO nanorods for methylene blue degradation. Ceramics International (45) 21430–21435, https://doi.org/10.1016/j.ceramint.2019.07.132.

Kröhnke, C., (2001) Encyclopedia of Materials: Science and Technology. Elseviers publishers

Kumar, R., Kumar, G., Al-Dossary, O., and Umar, A., (2015) ZnO nanostructured thin films: Depositions, properties and applications—A review. Mater. Express 2015, 5, 3–23. doi:10.1166/mex.2015.1204

Layth, M.A., (2014) Study the Effect of Annealing on Optical and Electrical Properties of ZnS Thin Film Prepared by CO2 Laser Deposition Technique. Iraqi J. Laser, (13), pp. 29-35.

Li, F., Wan, Y., Chen, J., Hu, X., Tsang, D.C., Wang, H., and Gao, B., (2020). Novel ball-milled biochar-vermiculite nanocomposites effectively adsorb aqueous As(V). Chemosphere, 260, 127566.

Liu, X., Pan, L., Zhao, Q., Lv, T., Zhu, G., Chen, T., Lu, T., Sun, Z., and Sun, C., (2011). UV assisted photocatalytic synthesis of ZnO–reduced graphene oxide composites with enhanced photocatalytic activity in reduction of Cr(VI). Chem. Eng. Journal, 183, 238–243. doi:10.1016/j.cej.2011.12.068.

Madkhali, N., (2022). Analysis of Structural, Optical, and Magnetic Properties of (Fe,Co) Co-Doped ZnO Nanoparticles Synthesized under UV Light. Condens. Matter, 7, 63. https://doi.org/10.3390/condmat7040063.

Martinson, A.B., Elam, J.W., Hupp, J.T., and Pellin, M.J., (2007). ZnO nanotube based dye-sensitized solar cells. Nano Lett ;7:2183.

Mbonu, J. I. (2015) Determination of Ni(II) crystal structure by powder x-ray diffraction. Scientia Africana, 14 (1), 158-164.

Mhadhbi, M., (2021). Modelling of the High-Energy Ball Milling Process. Advances in Materials Physics and Chemistry, 11, 31-44. https://doi.org/10.4236/ampc.2021.111004

Nada, M., (2010). Structural and Optical Properties of ZnS Thin Films Prepared by Spray Pyrolysis Technique, Department of Physics, College of Science, University of Baghdad, Baghdad-Iraq.

Noor H., Majeed A.H., and Ahmed H., (2019) Structural, Optical and Dielectric Properties of (PS- In2 O3 / ZnCoFe2 O4) Nanocomposites. Egyptian Journal of Chemistry. Egypt.J.Chem. V 62(2),577 – 592. DOI: 10.21608/ejchem..14646.1887.

Oluyamo S.S., and Agunbiade D.B., (2016). Spin coated Tin oxide thin film for optical and optoelectronic materials application. International Journal of innovated Research and Advanced studies (IJIRAS),3(8), 394-398.

Prerna, K., Anubhav, D., and Ratan, G., (2021). Nanoparticles: An Overview Drugs and Cell Therapies in Haematology (ISSN: 2281-4876) 10, (1), 1487 – 1497.

Rijesh, M., Aswin, D., Kapil, D.,. Surendranathan, A. O., and Sreekanth, M. S., (2018). Effect of Milling Time on Production of Aluminium Nanoparticle by High Energy Ball Milling, International Journal of Mechanical Engineering and Technology, 9(8), 646–652.

Rong, P., Ren, S., and Yu, Q., (2018). Fabrications and Applications of ZnO Nanomaterials in Flexible Functional Devices-A Review. Crit. Rev. Anal. Chem., 49, 336–349. https://doi.org/10.1080/10408347.2018.1531691.

Saleem A. H., Rashid O. K., and Sura N.T. (2016). Structural and optical properties of Tin Oxide and Indium doped SnO_2 thin films deposited by thermal evaporation technique. Journal of Advances in Physics, 12 (3), 4394-4399.

Satoshi, H., and Nick, S., (2013). Introduction to Nanoparticles. Microwaves in Nanoparticle Synthesis, First Edition. 1 – 24.

Schulz, B., (2021). Monazite Microstructures and Their Interpretation in Petrochronology. Front. Earth Sci. 9:668566. doi: 10.3389/feart.2021.668566.

Sutapa, I.W., Abdul W.W., Taba, P., and Nafie N. L., (2018) Dislocation, crystallite size distribution and lattice strain of magnesium oxide nanoparticles. IOP Conf. Series: Journal of Physics: Conf. Series (979)012021 doi :10.1088/1742-6596/979/1/012021.

Tan, X., Jaka, S., Wenrong, Y.,Yongbai, Y., Alexey, M., Glushenkov, Lu, H.L., ,Patrick, C., Howlettb, and Ying, C., (2013) Ball milling: a green mechanochemical approach for synthesis of nitrogen doped carbon nanoparticles. Nanoscale, 5, 7970. DOI: 10.1039/c3nr02328a.

Tereshchenko, A., Bechelany, M., Viter, R., Khranovskyy, V., Smyntyna, V., Starodub, N., and Yakimova, R., (2016) Optical biosensors based on ZnO nanostructures: Advantages and perspectives. A review. Sens. Actuators B Chem., 229, 664–677. https://doi.org/10.1016/j.snb.2016.01.099

Theerthagiri, J., Salla, S., Senthil, R.A., Nithyadharseni, P., Madankumar, A., Arunachalam, P., Maiyalagan, T., and Kim, H.S., (2019) A review on ZnO nanostructured materials: Energy, environmental and biological applications. Nanotechnology, 30, doi:10.1088/1361-6528/ab268a 392001.

Wang, R., Xin, J., and Tao, X., (2005). UV-blocking property of dumbbell-shaped ZnO crystallites on cotton fabrics. Inorg Chem ;44:3926.

Wanjala, K. S., Njoroge, W. K., and Ngaruiya, J. M. (2016). Optical and electrical characterization of ZnS: Sn thin films for solar cell application. Int. J. Energy Enginneering, 6(1).

Wei, Chen., Huang, H., Tian, B., and Shaoyong, J., (2017). Geochemistry of Monazite within Carbonatite Related REE Deposits. Resources, 6, 51; doi:10.3390/resources6040051.

Yakuphanoglu F., Barim G., and Erol I. (2007). The effect of $FeCl_3$ on the optical constants and optical band gap of MBZMA-CO-MMA polymer thin films. Physica B, 391, 136-140.

Yang, M., Wang, D., Peng, L., Xie, T., and Zhao, Y., (2006). Photoelectric response mechanisms dependent on RuN3 and CuPc sensitized ZnO nanoparticles to oxygen gas. Nanotechnology; 17:4567.

Zhang, N., Mao, Y., Wu, S., and Xu, W., (2022). Effects of the Ball Milling Process on the Particle Size of Graphene Oxide and Its Application in Enhancing the Thermal Conductivity of Wood. Forests 13, 1325. https://doi.org/10.3390/f13081325.